Generalized transfer matrix model for dipole radiation-dynamics modification in layered media: application to incoherent light-emitting structures in thin film geometry

Amade Ndiaye, Christian Seassal, Emmanuel Drouard, Badhise Ben Bakir

Research Article Vol. 2, No. 1 / 15 Jan 2023 / Optics Continuum 31
OPTICS CONTINUUM

Generalized transfer matrix model for dipole radiation-dynamics modification in layered media: application to incoherent light-emitting structures in thin film geometry

AMADE NDIAYE,[1,2] CHRISTIAN SEASSAL,[2] EMMANUEL DROUARD,[2] AND BADHISE BEN BAKIR[1,*]

[1] Univ. Grenoble Alpes, CEA, LETI, MINATEC Campus, CEA-Grenoble, F38054 Grenoble, France
[2] Univ. Lyon, Institut des Nanotechnologies de Lyon-INL, UMR CNRS 5270, CNRS, Ecole Centrale de Lyon, Ecully F-69134, France
[*] badhise.ben-bakir@cea.fr

Abstract: Incoherent light-emitting structures are of key interest for many fields in optoelectronics and spontaneous emission is the physical phenomenon underlying their light emission process. In this paper, we propose a novel full-matrix algebraic framework for modeling spontaneous emission modification from radiating electric dipoles in layered media. This formalism generalizes the standard 2×2 transfer-matrices into a compact 3×3 framework, which thus allows to treat dipole radiation directly into the matrix formulation as a source matrix. Its accuracy has been confirmed by incoherent 3D-FDTD. It has then been extended to complex emitter regions with both spectral and spatial distributions using incoherent combination. Finally, we applied this approach to various examples to demonstrate its applicability. Since it only requires modest computational efforts, we hope that this model can help better understand spontaneous emission dynamics in layered media and thus pave the way to novel design guidelines for devices in many fields of optoelectronics.

1. Introduction

Incoherent semiconductor light-emitting structures are of major interest for many applications in the field of optoelectronics, e.g., solid-state lighting, optical communication and displays [1]. The physical principle underlying light emission in those structures is spontaneous emission from radiating electric dipoles, stemming from electron-hole pairs that spontaneously recombine in certain regions of the devices [2]. The dynamics of this spontaneous emission mechanism can be strongly altered by the presence of an optical environment and those so-called cavity effects tend to get stronger as the devices get thinner [3]. Since more recent incoherent light-emitting structures such as multiple quantum well (MQW) color converters or ultrathin-film light-emitting diodes (LEDs) can have thicknesses on the order of magnitude of the wavelength [4,5], it is then of crucial interest to be able to thoroughly study dipole emission modification in layered media. Understanding all the related phenomena at play would thus ultimately help improve number of key performances of the thin-film devices such as light extraction efficiency (LEE), directionality, brightness, [3] etc.

Several formulations and models have been developed for that matter over the years, but the most recently used are derived from the work of Benisty et al. [3]. In that work, the authors unified in a single framework the spontaneous emission theory of Lukosz [6] and the already widely used transfer-matrix method [7]. Although the aforementioned approach has already been used for various types of devices, its implementation is often hindered by the 2×2 nature of the standard transfer-matrices. Indeed, due to this 2×2 framework, dipole emission could not be directly included into the matrix formalism (2×2 transfer-matrices are passive and cannot

#468231 https://doi.org/10.1364/OPTCON.468231
Journal © 2023 Received 21 Jun 2022; revised 6 Oct 2022; accepted 19 Oct 2022; published 3 Jan 2023

OPTICS CONTINUUM

embed a light source) and had thus to be separately treated as a discontinuity of the field across the source plane. This often led to complex analytic calculations, which could require additional computational efforts [8].

In this paper, we propose a novel full-matrix algebraic formalism for modeling dipole emission modification in layered media, wherein the standard transfer-matrices are generalized into a compact 3×3 framework allowing to directly treat dipole radiation as a source matrix. The paper is organized as follows. Section 2 outlines the plane-wave expansion method for treating spontaneous emission in an unbounded medium, while the 3×3 formalism is introduced in section 3. The generalized transfer-matrix model is then developed in sections 4 and 5 for stratified media and applied to some incoherent light-emitting structures in section 6.

2. Spontaneous emission in an unbounded medium

As mentioned above, electron-hole recombinations in semiconductor incoherent light-emitting devices can be modeled as radiating electric dipoles, whose emission rates depend on their orientation and the polarization of the emitted light. The orientation of the so-formed electric dipoles (set by their dipole moments) can be decomposed within a basis of mutually-orthogonal horizontal and vertical orientations. As shown by Lukosz in [6], a convenient way to represent the resulting dipole field is as a superposition of *s*- and *p*-polarized plane and evanescent waves. The radiation patterns of the emitters can thus be described both in the near- and farfield zones within this framework.

As shown in Fig. 1, vertical dipoles (denoted *v*) can only couple to *p*-polarized light with a normalized radiation pattern (power per unit solid angle) in an unbounded medium which reads as [9]:

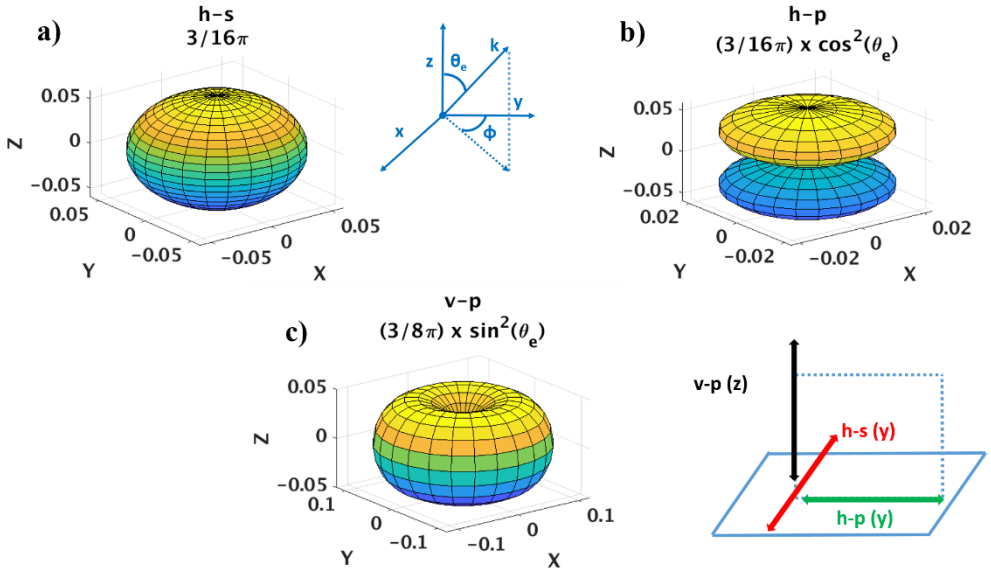

Fig. 1. Normalized radiation patterns of horizontal dipoles in a) s- and b) p-polarizations and of c) vertical dipoles in p-polarization, all lying in an unbounded medium.

$$\Pi_{\infty}^{v,p} = \frac{3}{8\pi} sin^2(\theta_e), \tag{1}$$

Here θ_e is the off-normal emission angle and subscript e refers to the emitter's medium.

OPTICS CONTINUUM

On the other hand, horizontal dipoles (denoted h) with arbitrary azimuthal angles can couple to both s- and p-polarized light. The corresponding normalized radiation patterns can be expressed as [10]:

$$\Pi_\infty{}^{h,s} = \frac{3}{16\pi}, \quad \Pi_\infty{}^{h,p} = \frac{3}{16\pi} cos^2(\theta_e). \tag{2}$$

The factors 3/8π and 3/16π are normalization factors so that the total powers through 4π sr for vertical dipoles in p-polarization on the one hand and for horizontal dipoles in (s + p) equal unity:

$$\int_{\theta=0}^{\theta=\pi} \int_{\varphi=0}^{\varphi=2\pi} \Pi_\infty{}^{v,p} \sin(\theta)\, d\theta d\varphi = 1, \tag{3}$$

$$\int_{\theta=0}^{\theta=\pi} \int_{\varphi=0}^{\varphi=2\pi} \left(\Pi_\infty{}^{h,s} + \Pi_\infty{}^{h,p}\right) \sin(\theta)\, d\theta d\varphi = \frac{3}{4} + \frac{1}{4} = 1. \tag{4}$$

We can note that for horizontal dipoles in an unbounded medium the ratio between the total powers in s- and p-polarization is 3:1. The radiation patterns as well as the dipole orientations and field polarizations are depicted in Fig. 1.

For a completely isotropic light source, those power flows are combined as follows [3]:

$$\Pi_\infty{}^{iso} = \frac{1}{3}\Pi_\infty{}^{v} + \frac{2}{3}\Pi_\infty{}^{h} = \frac{1}{4\pi}, \tag{5}$$

Here:

$$\Pi_\infty{}^{v} = \Pi_\infty{}^{v,p}, \quad \Pi_\infty{}^{h} = \Pi_\infty{}^{h,s} + \Pi_\infty{}^{h,p}. \tag{6}$$

As expected we end up with a spherical emission as shown by Eq. (5) and in Fig. 2.

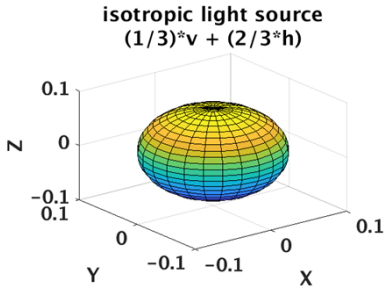

Fig. 2. Normalized radiation pattern of an isotropic light source in an unbounded medium.

3. 3×3 formalism in an unbounded medium

In this section, we introduce our generalized 3 × 3 transfer-matrix formalism for the simple case of a dipole in an unbounded medium. Figure 3 (a) depicts a schematics of the dipole source in an unbounded medium with the different parameters used in this development. We consider an emitter at a position z_p. The normalized source terms for forward- and backward-propagation are denoted S_A and S_B, respectively. We also consider two arbitrary positions (z_1 and z_2) on both sides of the dipole. The corresponding electric field amplitudes are given in Fig. 3 (b).

OPTICS CONTINUUM

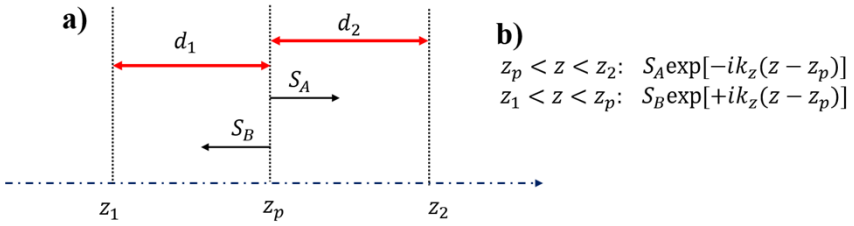

Fig. 3. a) Schematics diagram of a dipole source at a position z_p in an unbounded medium. z_1 and z_2 are 2 positions at distances of d_1 and d_2 from the source, respectively. S_A and S_B are the amplitudes of the forward- and backward-propagating source terms. b) Expressions of the electric-field amplitudes on both sides of the dipole.

In this context, we can write the relationship between the electric fields and the source terms by using the standard 2×2 transfer matrix formalism:

$$\begin{pmatrix} {E_1}^+ \\ {E_1}^- \end{pmatrix} = \begin{pmatrix} \exp(ik_z d_1) & 0 \\ 0 & \exp(-ik_z d_1) \end{pmatrix} \begin{pmatrix} {E_p}^+ - S_A \\ {E_p}^- \end{pmatrix}, \tag{7}$$

$$\begin{pmatrix} {E_p}^+ \\ {E_p}^- \end{pmatrix} = \begin{pmatrix} \exp(ik_z d_2) & 0 \\ 0 & \exp(-ik_z d_2) \end{pmatrix} \begin{pmatrix} {E_2}^+ \\ {E_2}^- + S_B \exp(ik_z d_2) \end{pmatrix}, \tag{8}$$

Here k_z is the complex z-wave-vector component such as $k_z/k = cos(\theta_e)$, e referring to the emitter medium. E_j represents the electric field amplitude at the position z_j. The superscripts + (-) designate the forward- (backward-) propagating electric fields.

Considering now a 3×3 formalism where the electric-field vectors have 3 components instead of 2 and combining Eq. (7) and Eq. (8), we can write a more generalized formalism as:

$$\begin{pmatrix} {E_1}^+ \\ {E_1}^- \\ 1 \end{pmatrix} = P^e(d_1) S P^e(d_2) \begin{pmatrix} {E_2}^+ \\ {E_2}^- \\ 1 \end{pmatrix}, \tag{9}$$

Here $P^j(d_j)$ and S account for the propagation matrix in the layer (or medium in this case) denoted j over a distance d_j and the source matrix, respectively. They are expressed as:

$$P^e(d_j) = \begin{pmatrix} \exp(ik_z d_j) & 0 & 0 \\ 0 & \exp(-ik_z d_j) & 0 \\ 0 & 0 & 1 \end{pmatrix}, \tag{10}$$

$$S = \begin{pmatrix} 1 & 0 & -S_A \\ 0 & 1 & +S_B \\ 0 & 0 & 1 \end{pmatrix}. \tag{11}$$

The main advantage of the herein-developed formalism appears thus clearly, since it eliminates the need to resort to discontinuity equations for including dipole emission inside the calculations. It indeed provides (see Eq. (9)) a full-matrix formulation which directly relates the electric fields

OPTICS CONTINUUM

at any positions on both sides of the dipole source. This feature makes it easier to implement numerically with less analytical calculations and more modest computing efforts. In addition, its compact nature (one equivalent matrix for the whole system) facilitates the physical interpretations of the performances of the corresponding devices as we will see later on.

Let us note that in this formalism and contrary to standard implementations of models for dipole emission modification [3], the sign differences between the forward- and backward-propagating source terms are already accounted for in Eqs. (7),(8). We can also emphasize that the third component of the electric field which is set to 1 is merely a mathematical trick to enable the generalization.

In the following sections, this novel 3×3 transfer-matrix formulation will be implemented for dipole emission in stratified media.

4. Spontaneous emission in layered media

In this section, we develop the previous generalized transfer-matrix model for dipole emission in a multilayer structure. We choose a typical incoherent light-emitting structure made up of a stack of layers assumed to be homogeneous. All layers in the structure are considered infinite in xy plane and with a finite thickness (along z). The dipole emitter is represented as a source plane which lies at a position z_{ext} within an emission layer referred to as e, with a thickness of d_e. S_A and S_B represent the normalized forward- and backward-propagating source terms basically given by the square roots of the radiation patterns provided in Eqs. (1),(2). In our model, since the sign differences between the forward- and backward-propagating source terms are already accounted for, we have $S_A = S_B$. We will keep S_A and S_B thereafter for the sake of clarity.

The normalized source terms in the three basic configurations are provided in Table 1.

Table 1. Normalized source terms for horizontal and vertical dipoles

Dipole orientation	s-polarized light	p-polarized light
Horizontal	${S_A}^{h,s} = {S_B}^{h,s} = \sqrt{\frac{3}{16\pi}}$	${S_A}^{h,p} = {S_B}^{h,p} = \sqrt{\frac{3}{16\pi}}\cos(\theta_e) = \sqrt{\frac{3}{16\pi}}\frac{k_{z,e}}{k_e}$
Vertical	${S_A}^{v,s} = {S_B}^{v,s} = 0$	${S_A}^{h,p} = {S_B}^{h,p} = \sqrt{\frac{3}{8\pi}}\sin(\theta_e) = \sqrt{\frac{3}{8\pi}}\frac{k_{//,e}}{k_e}$

Here $k_{z,e}$ $(k_{//,e})$ accounts for the z- (in-plane) -wave-vector component inside the emission layer. We can note that evanescent modes can also be accounted for by letting $k_{z,e}$ run along the imaginary axis and go from $i0$ to $+i\infty$. We can also note that the source terms are dipole-orientation- and polarization-dependent and so will be all the resulting fields. In the following, the superscripts *h, v, s and p* will be dropped for the sake of clarity.

$E_{A(B)}$ represents the electric field on right (left) side of the source plane (source terms modified by the optical environment). The superscripts +(-) still designate the forward-(backward-) propagating fields.

The multilayer structure is sandwiched between two semi-infinite ambient media (denoted *1* and *2*) where light will be extracted. The refractive indices of the ambient media as well as the emission layer are denoted $n_{1(2)}$ and n_e, respectively. The matrices R and L depict the propagation from the ambient medium 2 up to the right interface of the emission layer and from the left interface of the emission layer to ambient medium 1, respectively. Since there are no fields propagating from the ambient media into the structure, the boundary conditions can be written as ${E_1}^{+}={E_2}^{-}=0$.

The multilayer structure and all the corresponding parameters are depicted in Fig. 4.

OPTICS CONTINUUM

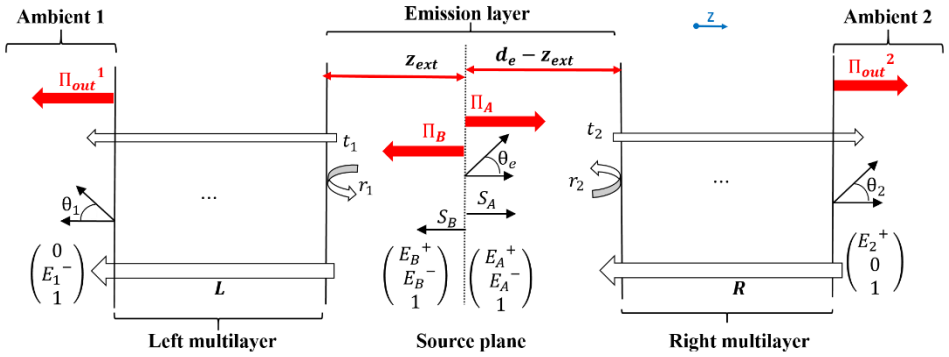

Fig. 4. Schematics depicting a multilayer structure enclosed with semi-infinite ambient media. The emitter is represented as a source plane within the emission layer.

Using the generalized transfer-matrix model described in the previous section (Eq. (9)), we can now write:

$$\begin{pmatrix} 0 \\ E_1^- \\ 1 \end{pmatrix} = M \begin{pmatrix} E_2^+ \\ 0 \\ 1 \end{pmatrix} = \begin{pmatrix} M_{11} & M_{12} & M_{13} \\ M_{21} & M_{22} & M_{23} \\ 0 & 0 & 1 \end{pmatrix} \begin{pmatrix} E_2^+ \\ 0 \\ 1 \end{pmatrix}, \tag{12}$$

Here M is the equivalent matrix of the whole structure (including dipole emission) and reads as:

$$M = LP^e(z_{ext})SP^e(d_e - z_{ext})R. \tag{13}$$

$P^e(z_{ext})$ and $P^e(d_e\text{-}z_{ext})$ are the propagation matrices inside the emission layer over distances of z_{ext} and $d_e\text{-}z_{ext}$ as in Eq. (10). S is the source matrix whose expression is provided in Eq. (11).

Let us recall that the source matrix S depends on both dipole orientation and light polarization, while the propagation (and interface) matrices are only polarization-dependent.

In the following sections, we are going to derive the expressions of the electric fields outside and inside the structures in order to determine key figure of merits (FoM) of light-emitting structures such as LEE, directionality through the farfield emission patterns, Purcell factor, etc.

4.1. Determination of the external fields

The implementation of the model starts by considering an angle inside the emission layer θ_e ranging from 0 to π/2. Afterwards, once the equivalent matrix M has been calculated using Eq. (13), one needs to derive the fields in the ambient media (external fields) at all corresponding external angles $\theta_{1(2)}$ including evanescent waves (complex angles).

Using Eq. (12), one can easily find that the external fields are expressed as:

$$E_2^+ = -\frac{M_{13}}{M_{11}}, \quad E_1^+ = \frac{M_{23}M_{11} - M_{21}M_{13}}{M_{11}}. \tag{14}$$

For the physical interpretation of these formulas to become clearer, let us introduce r_1 (r_2) and t_1 (t_2) which designate the complex Fresnel reflection and transmission coefficients for all layers on the left (right) side combined as depicted in Fig. 4. Using the elements of matrices L and R,

OPTICS CONTINUUM

these coefficients express as [11]:

$$r_1 = -\frac{L_{12}}{L_{11}}, \qquad r_2 = \frac{R_{21}}{R_{11}},$$
$$t_1 = \frac{L_{22}L_{11} - L_{12}L_{21}}{L_{11}}, \qquad t_2 = \frac{1}{R_{11}}. \tag{15}$$

After detailing the expressions in Eq. (14) using the elements of the equivalent matrix M and combining them with Eq. (15), one can find new expressions for the external fields as in [8]:

$$E_2{}^+ = \frac{t_2(S_A e^{-ik_{z,e}(d_e - z_{ext})} + r_2 S_B e^{-ik_{z,e}(d_e + z_{ext})})}{1 - r_1 r_2 e^{-ik_{z,e}2d_e}},$$
$$E_1{}^- = \frac{t_1(r_2 S_A e^{-ik_{z,e}(2d_e - z_{ext})} + S_B e^{-ik_{z,e}z_{ext}})}{1 - r_1 r_2 e^{-ik_{z,e}2d_e}}. \tag{16}$$

The physical meaning of these formulas is now clearer. For instance, the outgoing field on the right ($E_2{}^+$) stems from the right-going source term propagated into the right side the emission layer, added to the left-going source term reflected off the left side of the structure, which are both transmitted through the right side of the structure.

The common denominator in both cases denoted Δ is intrinsic to the structure and carries its modal properties. Indeed by definition, a lossless guided wave will satisfy the unity round-trip condition [3]:

$$r_1 r_2 e^{-ik_{z,e}2d_e} = 1. \tag{17}$$

Thus, the denominator Δ will equal zero at certain discrete angles and the fields in Eq. (16) will diverge, making it impossible to directly take into account guided modes. The numerical trick to calculate the evanescent fields whose internal fields correspond to guided modes is to introduce damping layers, which are ultrathin artificial absorbing layers, at each side of the source plane as suggested in [3].

Let us note that the propagation matrices into those damping layers have now to be taken into account in the final expression of the equivalent matrix. Equation (13) turns thus into:

$$M = LP^e(z_{ext})P^{DL}(d_{DL})SP^{DL}(d_{DL})P^e(d_e - z_{ext})R. \tag{18}$$

Here the superscript DL designates the damping layers and d_{DL} represents their thickness. Details about the parameters to implement those damping layers will be provided in subsection 6.1.1.

4.2. Derivation of the internal fields and power fluxes

From the external fields, it is possible to determine the electric fields at any position inside the multilayer structures using the proper propagation and interface matrices. For instance, it can be of particular interest to calculate the internal fields inside the emissive layer on both sides of the source plane. Indeed for incoherent light-emitting structures, it can provide the spontaneous emission distribution among guided modes, which is of major interest to design highly directional emitters [4].

OPTICS CONTINUUM

Using the propagation matrices of the previous section, the internal fields can be expressed as:

$$\begin{pmatrix} {E_A}^+ \\ {E_A}^- \\ 1 \end{pmatrix} = P^e(d_e - z_{ext})R \begin{pmatrix} {E_2}^+ \\ 0 \\ 1 \end{pmatrix}, \tag{19}$$

$$\begin{pmatrix} {E_B}^+ \\ {E_B}^- \\ 1 \end{pmatrix} = (P^e(z_{ext}))^{-1}L^{-1} \begin{pmatrix} 0 \\ {E_1}^- \\ 1 \end{pmatrix}. \tag{20}$$

Following that, one can easily find that the resulting angular distributions of the internal emission Π_A and Π_B on both sides of the source plane depicted in Fig. 4 read as (using the Poynting vector flux):

$$\Pi_A = \frac{d{P_{in}}^A}{d{\Omega_{in}}^A} = \left|{E_A}^+\right|^2 - |{E_A}^-|^2, \tag{21}$$

$$\Pi_B = \frac{d{P_{in}}^B}{d{\Omega_{in}}^B} = \left|{E_B}^+\right|^2 - |{E_B}^-|^2. \tag{22}$$

Spontaneous emission dynamics can be heavily affected by the optical environment as mentioned above. The Purcell factor denoted F_P is thus a key FoM since it represents the modification (enhancement or inhibition) of the total spontaneous emission rates inside the structure as compared to dipole emission rates in an unbounded medium. As all the electric fields are already normalized, the Purcell factor can be directly evaluated as:

$$F_P = \int_{\theta_e=0}^{\theta_e=\frac{\pi}{2}} \int_{\varphi=0}^{\varphi=2\pi} (\Pi_A + \Pi_B) \sin(\theta_e)\, d\theta_e d\varphi. \tag{23}$$

Last but not least, we can note that Eq. (21) and Eq. (22) are very easy to implement numerically, but do not picture the physics of the coupling between spontaneous emission and the cavity modes. As shown in [12], a more convenient way to express the angular internal emission and better understand each phenomenon at play is as follows (for example on the left side of the source plane):

$$\Pi_B = \xi_B \times \mathcal{A}_B \times \Pi_\infty, \tag{24}$$

The internal emission is thus set by three main factors: the Airy function $\mathcal{A}_B$ which accounts for the resonant behavior of the bare Fabry-Pérot (FP) cavity, the antinode factor ξ_B which represents the coupling efficiency between spontaneous emission and the cavity modes and Π_∞ which is the dipole radiation in an unbounded medium provided in Eqs. (1),(2). Similar expressions can be given for Π_A. In our framework, the Airy function and antinode factor can be expressed as:

$$\xi_B = |1 + r_2 \exp(-ik_{z,e}2(d_e - z_{ext}))|^2 = |1 + r_2 \exp(-i\varphi_c)|^2. \tag{25}$$

$$\mathcal{A}_B = \frac{1 - |r_1|^2}{|1 - r_1 r_2 \exp(-ik_{z,e}2d_e)|^2} = \frac{1 - |r_1|^2}{\Delta^2}. \tag{26}$$

Here the phase shift φ_c will eventually set the coupling efficiency between dipole emission and the cavity modes. Furthermore, as we have mentioned in subsection 4.1, the denominator of the Airy function Δ^2 carries the modal properties of the structure. For instance, as we will see later on, its zeros provide the discrete angular positions of the guided modes supported by the cavity.

More details about those factors will be provided in the application examples of section 6.

OPTICS CONTINUUM

4.3. Farfield emission patterns and light extraction efficiency

Directionality and LEE are key FoM for designing incoherent light-emitting structures [13]. The former depends on the shape of the radiation pattern in the ambient media, while the latter is set by the ratio between the total extracted and emitted powers.

To evaluate the farfield patterns in the outside media (ambient 1 and 2), one has to take into account the change in solid angles when going out of the multilayer structure due to refraction. By definition, the farfield pattern in the outer ambient media (e.g. Ambient 1) denoted $\Pi_{\text{out}}{}^{1}$ reads as:

$$\Pi_{out}{}^{1} = \frac{dP_{out}{}^{1}}{d\Omega_{out}{}^{1}} = \frac{dP_{out}{}^{1}}{dP_{in}{}^{B}} \times \frac{d\Omega_{in}{}^{B}}{d\Omega_{out}{}^{1}} \times \frac{dP_{in}{}^{B}}{d\Omega_{in}{}^{B}}, \tag{27}$$

The first factor is the power transmission coefficient between the emission layer and the outer medium 1. Using the flux of the Poynting vector as in [8], it can be written:

$$\frac{dP_{out}{}^{1}}{dP_{in}{}^{B}} = \frac{\vec{S}^{1}_{out}.\,\vec{A}^{1}_{out}}{\vec{S}^{B}_{in}.\,\vec{A}^{B}_{in}} = \frac{n_1 |E_1{}^{-}|^2 cos(\theta_1)}{n_e(|E_B{}^{+}|^2 - |E_B{}^{-}|^2) cos(\theta_e)}, \tag{28}$$

Here $\vec{S}^{B}_{in}$ and $\vec{S}^{1}_{out}$ represent the Poynting vectors in the emission layer and the outer ambient medium 1, respectively. In addition, $\vec{A}^{B}_{in}$ and $\vec{A}^{1}_{out}$ are unit vectors normal to the surface for the emission layer and the ambient medium 1, respectively.

The second factor accounts for the change in solid angle due to refraction. After an angular differential of the Snell-Descartes' law $n_e \sin(\theta_e) = n_1 \sin(\theta_1)$, one can get [14]:

$$d\Omega_{in}{}^{B} = \sin(\theta_e) d\theta_e d\varphi_e = \frac{n_1{}^{2} cos(\theta_1)}{n_e{}^{2} cos(\theta_e)} d\Omega_{out}{}^{1}, \tag{29}$$

Lastly, the third factor is the internal power flux given in Eq. (22).

Combining Eq. (27–29), we find the expressions for the farfield emission patterns on each side of the ambient medium:

$$\Pi_{out}{}^{1(2)} = \frac{dP_{out}{}^{1(2)}}{d\Omega_{out}{}^{1(2)}} = \left|E_{1(2)}{}^{-}\right|^2 \frac{n_{1(2)}{}^{3} cos^2\left(\theta_{1(2)}\right)}{n_e{}^{3} cos^2\left(\theta_e\right)}. \tag{30}$$

Let us recall that after the external fields have been calculated using Eq. (14), one has to drop the evanescent waves (complex outside angles) and only consider outside angles $\theta_{1(2)}$ ranging from 0 to $\pi/2$. Once the farfield patterns have been calculated, by definition LEE can be written as:

$$LEE_{1(2)} = \frac{\int_{\theta_{1(2)}=0}^{\theta_{1(2)}=\frac{\pi}{2}} \int_{\varphi=0}^{\varphi=2\pi} \Pi_{out}{}^{1(2)} \sin\left(\theta_{1(2)}\right) d\theta_{1(2)} d\varphi}{F_P}. \tag{31}$$

5. Incoherent combination for extension to complex emitter regions

In the previous section, the generalized transfer-matrix model has been developed for a single monochromatic dipole source-plane to provide the basic formulas that can be used for its implementation. Real-life devices often include distributed dipoles, an emission spectrum, etc. In the following, we provide the formulas taking into account those considerations.

5.1. Completely isotropic dipoles

In a semiconductor light-emitting structure, emitter orientations are set by the dipole moments of the radiating electric dipoles, which depend on the carrier confinement conditions. The simplest case is the completely isotropic light source (e.g. bulk semiconductors), where emitters are

OPTICS CONTINUUM

arbitrarily oriented (isotropic distribution). In that case, only one third of the emitted light comes from the vertical dipoles. Thus, the internal power flow and farfield pattern, here denoted Π_{int} and Π_{out} for the sake of clarity, are combined using the following weighted averages:

$$\begin{aligned}
{\Pi_{int(out)}}^{combined} &= \tfrac{1}{3}{\Pi_{int(out)}}^{v} + \tfrac{2}{3}{\Pi_{int(out)}}^{h},\\
{\Pi_{int(out)}}^{v} &= {\Pi_{int(out)}}^{v,p},\\
{\Pi_{int(out)}}^{h} &= {\Pi_{int(out)}}^{h,s} + {\Pi_{int(out)}}^{h,p}.
\end{aligned} \tag{32}$$

LEE follows the same procedure, but for horizontal dipoles *s*- and *p*-polarized light need to be averaged taking into account their different radiation dynamics through the Purcell factor (F_P). Thus, LEE expresses as:

$$\begin{aligned}
LEE^{combined} &= \tfrac{1}{3}LEE^{v} + \tfrac{2}{3}LEE^{h},\\
LEE^{v} &= LEE^{v,p},\\
LEE^{h} &= \frac{LEE^{h,s}\times {F_P}^{h,s} + LEE^{h,p}\times {F_P}^{h,p}}{{F_P}^{h,s} + {F_P}^{h,P}}.
\end{aligned} \tag{33}$$

Let us recall (see section 2) that in an unbounded medium, ${F_P}^{h,s} = 3/4$ and ${F_P}^{h,p} = 1/4$.

More generally, depending on the structure the factors 1/3 and 2/3 might need to be adjusted. For instance in the case of quantum wells where light is often predominantly in-plane polarized [15], the contribution of vertical dipoles could be dropped.

5.2. Spatially distributed incoherent dipoles

The spatial distribution of the dipoles has to be considered in cases where the emitters are embedded within a layer whose dimensions are not negligible compared to the wavelength. In some structures, there can even be multiple sets of layers embedding the dipoles [16]. To treat these cases, one has to recall the incoherent nature of the spontaneous emission process. Indeed, there are not any interferences between light generated by different dipoles in those structures.

Assuming a uniform carrier distribution within the emission layer, the results for each emitter need then to be incoherently combined and read as:

$$\begin{aligned}
{\Pi_{int(out)}}^{combined} &= \frac{\sum_{z_{ext}=z_{ext,1}}^{z_{ext}=z_{ext,N}} \Pi_{int(out)}(z_{ext})}{N}.\\
LEE^{combined} &= \frac{\sum_{z_{ext}=z_{ext,1}}^{z_{ext}=z_{ext,N}} LEE(z_{ext})}{N}
\end{aligned} \tag{34}$$

Here, N is the number of dipole source-planes inside the emission layer and $z_{ext,j}$ accounts for the position of the emitter labelled j (see Fig. 4). Non-uniform carrier distributions can also be taken into account by weighting those equations by the emitter concentration along z considering simple models with the diffusion length as in [14].

5.3. Spectral broadening

Real-life incoherent light-emitting structures can have non-negligible full width at half-maximum (FWHM), thus their emission line shape should be considered in the model. Let us consider the source intrinsic spectrum denoted I_{in}, non-zero only between λ_{min} and $\lambda_{\max}$. By incoherently combining the results at each wavelength weighted by the intrinsic emission spectrum, the internal

OPTICS CONTINUUM

emission, farfield patterns and LEE read as:

$$\begin{aligned}
\Pi_{int}{}^{combined}\left(\theta_e\right) &= \frac{\int_{\lambda=\lambda_{min}}^{\lambda=\lambda_{max}} I_{in}(\lambda)\Pi_{int}(\lambda,\theta_e)d\lambda}{\int_{\lambda=\lambda_{min}}^{\lambda=\lambda_{max}} I_{in}(\lambda)d\lambda}.\\
\Pi_{out}{}^{combined}\left(\theta_{1(2)}\right) &= \frac{\int_{\lambda=\lambda_{min}}^{\lambda=\lambda_{max}} I_{in}(\lambda)\Pi_{out}\left(\lambda,\theta_{1(2)}\right)d\lambda}{\int_{\lambda=\lambda_{min}}^{\lambda=\lambda_{max}} I_{in}(\lambda)d\lambda}.\\
LEE^{combined} &= \frac{\int_{\lambda=\lambda_{min}}^{\lambda=\lambda_{max}} I_{in}(\lambda)LEE(\lambda)d\lambda}{\int_{\lambda=\lambda_{min}}^{\lambda=\lambda_{max}} I_{in}(\lambda)d\lambda}.
\end{aligned} \tag{35}$$

Although the combined farfield patterns are of key interest, they do not always provide a good insight into the behavior of each wavelength, which can be useful for structures with strong cavity effects [17]. In that sense, one could resort to the so-called spectrally-resolved farfield (SRF) where the weight of each wavelength is taken into account but without the sum. It can thus be written as:

$$SRF\left(\lambda,\theta_{1(2)}\right) = \frac{I_{in}\left(\lambda\right)\Pi_{out}\left(\lambda,\theta_{1(2)}\right)}{\int_{\lambda_i=\lambda_{min}}^{\lambda_i=\lambda_{max}} I_{in}\left(\lambda_i\right)d\lambda_i}, \tag{36}$$

Last but not least, the output spectrum denoted I_{out} can subsequently be calculated by integrating SRF over angles:

$$I_{out}(\lambda) = \int_{\theta_{1(2)}=0}^{\theta_{1(2)}=\frac{\pi}{2}} \int_{\varphi=0}^{\varphi=2\pi} SRF(\lambda,\theta_{1(2)})\sin(\theta_{1(2)})d\theta_{1(2)}d\varphi. \tag{37}$$

As we will see in the application examples of section 6, for some structures the outgoing light can experience a spectral redistribution which can lead to an altered output spectrum compared to the intrinsic spectrum.

5.4. Summary of the implementation procedure

In Fig. 5, we provide a detailed flow chart summarizing the numerical implementation of the herein-developed model. The full-matrix formalism helps make it very convenient. We can note (as mentioned above) that the equivalent matrix M needs to be established for both polarizations. When one changes the dipole orientation from vertical to horizontal, only the source matrix S will then need to be changed. In addition, one could easily transform the transfer-matrix formalism into a scattering-matrix ones using base changes for more stability particularly when simulating thick absorptive materials.

It is finally worth noticing that all the incoherent combinations given in section 5 can be considered as post-processing results. Depending on the applications, this model can provide LEE, farfield emission patterns (and therefore directionality), Purcell factors, photonic weights (fraction of the guided energy carried by each cavity mode), etc. This makes it a key tool for designing incoherent light-emitting structures.

OPTICS CONTINUUM

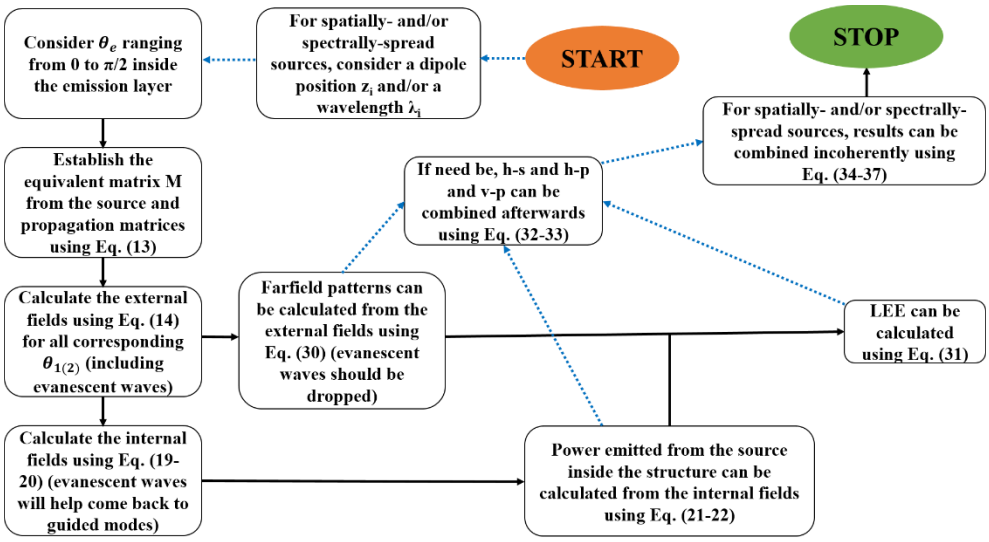

Fig. 5. Detailed flow chart of the implementation procedure.

6. Application examples

In this section, we wish to demonstrate the validity of the herein-developed model and its applicability to various types of light-emitting structures. For this purpose, we consider a high-index slab in different configurations. Figure 6 depicts the basic configuration of the following examples.

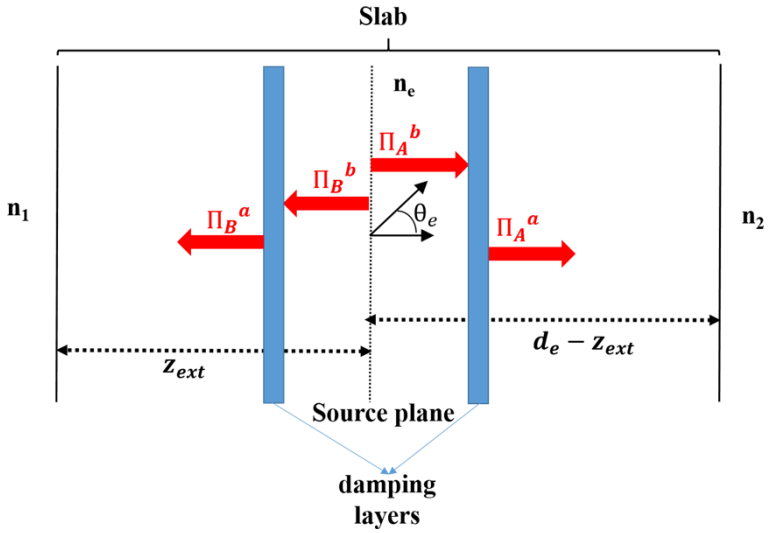

Fig. 6. Schematics of the high-index slab surrounded by semi-infinite ambient media (not at scale). The superscripts b and a designate the positions before and after the damping layers.

A high-index slab with a thickness d_e and a refractive index n_e is surrounded by two ambient semi-infinite media with refractive indices n_1 and n_2. We choose $n_e = 3$ for the examples. A dipole emitter (source plane) is placed at a distance z_{ext} from the left interface. As mentioned

OPTICS CONTINUUM

above, the numerical trick to account for guided modes in our calculations is to introduce two identical damping layers on both sides of the emitter to preserve symmetry. Those damping layers need to be thin enough (e.g. $\lambda/10^3$) not to modify direct light emission and close enough to the source (e.g. $\lambda/10^6$) to have the same coupling to guided modes [3]. Their complex refractive index is denoted $n_{DL} = n_{DL}' + in_{DL}''$, with n_{DL}' and n_{DL}'' designating the real ($n_{DL}' = n_e$) and imaginary parts (directly related to the absorption coefficient). The imaginary part will be referred to as the extinction coefficient in the following. This configuration will hold for examples in subsections 6.1 and 6.2.

6.1. High-index slab placed in vacuum

First, the high-index slab is placed in vacuum ($n_1 = n_2 = 1$). We are going to progressively implement complexity in this single slab to better understand the physics underlying light emission in incoherent light-emitting structures.

6.1.1. Convergence study and accuracy

The most basic configuration that can be used for simulating light-emitting structures is the case of the single monochromatic source-plane. In this section, we consider a horizontal monochromatic dipole (denoted h) located in the middle of the slab ($z_{ext} = d_e/2$). The slab thickness is chosen to be $n_e d_e/\lambda = 2.1$ as in [3] for the sake of comparison.

We first perform a convergence study to determine the extinction coefficient of the damping layers. Indeed, this can be tricky because it needs to be high enough for the guided power to couple into the damping layers, but not to start modifying the direct emission.

Figure 7(a) shows fractions of the total s-polarized light that are guided and extracted (on both sides of the slab). As we can see, when the extinction coefficient is less than $\sim 10^{-4}$, the damping layers are not sufficiently absorbing to couple the guided modes. Thus all the light is artificially extracted (LEE$\sim$100%), which provides incorrect results. We can note that guided modes still exist in this case, but cannot be accounted for due to the low values of the extinction coefficients. Next, the guided fraction increases with the extinction coefficient until it saturates, which shows the importance of the convergence study. Convergence is reached for extinction coefficients over $\sim 10^{-1}$, which means that power injected into guided modes goes necessarily into the damping layers. We can also note that the saturation value of LEE ($\sim$21%) is in agreement with the one found in [3] for a similar structure but with a different approach.

For the following simulations, the extinction coefficient of the damping layers is set to 10^{-1}. To further confirm this consideration, we calculated (see Fig. 7(b)) the internal power flux for s-polarized light before and after the damping layers (denoted by the superscripts a and b in Fig. 6). As expected from the reduced slab optical thickness, the emitted light outside the extraction cone (for $\theta_e > 20°$) couples to two guided modes depicted by two sharp peaks at $\sim$52.6° and $\sim$78.2°. We can see that the damping layers absorb all the power coupled into guided modes (e.g. peak intensities go from $\sim 10^2$ to 10^{-10} before and after the damping layers). It is also worth noticing that the direct emission (inside the air cone) is not impacted by those damping layers. Therefore, the imbalance between the power-fluxes at any locations before and after the damping layers will provide the power injected into guided modes. Curves with similar shapes are obtained for p-polarized light, albeit with different values.

To verify the accuracy of this generalized transfer-matrix model, we perform rigorous electromagnetic simulations using incoherent 3D-FDTD from commercially available software (FullWAVE and LED Utility from the Rsoft Design Suite) [1]. For the FDTD simulations, the lateral dimensions of the computation domain were fixed at 4μm and surrounded by perfectly matched layers (PML). In addition, the mesh sizes along all the spatial directions are set to 10nm.

Figure 8 depicts the combined total LEE (on both sides of the structure) and Purcell factor as a function of the reduced slab thickness for both the model and 3D-FDTD. For this comparison,

OPTICS CONTINUUM

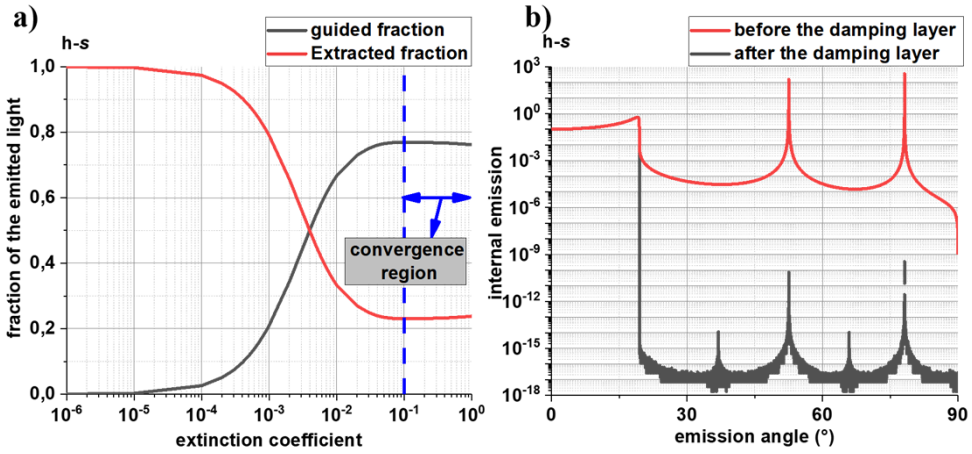

Fig. 7. s-polarized light from a single monochromatic horizontal dipole centered in a high-index slab. a) Extracted and guided fraction of the total emitted light as a function of the extinction coefficient of the damping layers. b) Angular internal emission per unit solid angle before and after the damping layers with an extinction coefficient of 10^{-1}.

results from both *s*- and *p*-polarization from a centered horizontal dipole have been combined using Eqs. (32),(33).

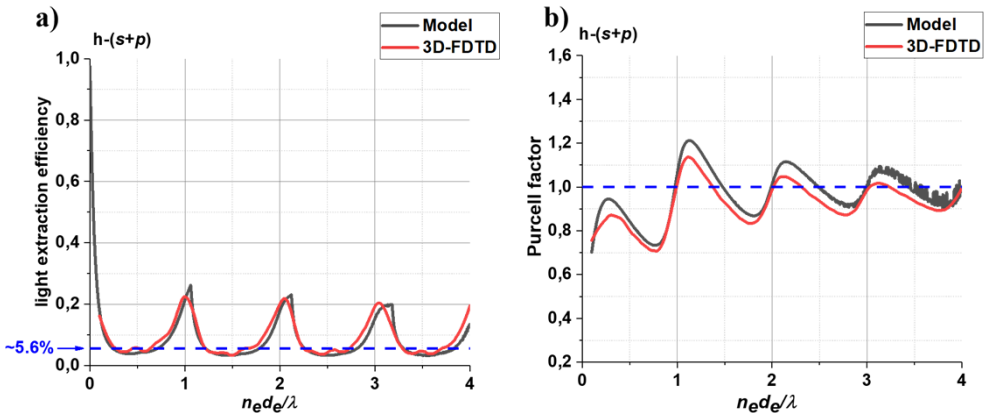

Fig. 8. Single horizontal dipole centered in a high-index slab. s- and p-polarization combined. a) LEE and b) Purcell factor as a function of the reduced thickness. The blue dashed line indicates the asymptotic values of LEE and Purcell factor.

Both results are in agreement with each other, which confirms the accuracy of the herein-developed model. As expected, spontaneous emission dynamics strongly depends on the reduced slab optical thickness through the Purcell factor and LEE. These variations match very well those obtained by Benisty et al. in [3]. Indeed, as the optical slab thickness increases, new guided modes successively exceed their cutoff conditions. As shown in [18], those modes most efficiently couple the emitted light a little above their cutoff conditions, which causes both LEE and Purcell factor to oscillate. It is worth noticing that the standardly used formula approximating LEE as the fraction of solid angles below critical angle (blue dashed lines in Fig. 8) [2] does not hold for structures with low cavity orders. Indeed, it only holds asymptotically for very high

OPTICS CONTINUUM

reduced thicknesses ($n_e d_e/\lambda > 20$) as shown in [3]. In that particular case, modes would become so numerous that the aforementioned effect would start to smear out.

It thus appears that when convergence is reached, the herein-developed model is well in agreement with rigorous electromagnetic simulations, which validates its accuracy.

6.1.2. Monochromatic distributed emitters

In the previous example, we only considered the simplest case of a single centered dipole, which has been the most used configuration so far when simulating dipole emission in incoherent light-emitting structures [19]. However, real-life devices often contain multiple emitters embedded in the so-called active region. Thus in some cases, one might need to account for the spatial distribution of the dipole source-planes (along z). In this section, we investigate the extent to which the single-centered-dipole approximation remains valid despite the presence of distributed emitters inside the structure and highlight some design rules for incoherent light-emitting devices.

For this example, we keep the same architecture as in the previous subsection. However, instead of a single emitter centered in a slab, we consider a realistic case of five horizontal dipoles regularly spaced of 10nm (two on every side of the centered dipole) [20]. We assume that the layer embedding the dipoles has the same refractive index as the slab. Except with the internal emission, *s*- and *p*-polarizations are combined using the equations provided in section 5. In this example, only light going out in the ambient layer 1 is considered (see Fig. 6).

Figure 9(a) shows the spontaneous emission distribution for *s*-polarized light as a function of the effective index for a single centered dipole and for the 5 emitters composing the active region. For the latter case, the results are incoherently combined using the equations provided in section 5.2. In the case of a single dipole, only even modes are excited since the dipole is placed at a node of the odd modes. However, when the whole emitter distribution is accounted for, odd modes start to couple to spontaneous emission as evidenced by the additional sharp peaks that occur when the 5 emitters are considered. This can be understood as follows. From Eq. (26–28), we have seen that among the three factors that set the internal power flux, only the antinode factor depends on the position of the source. Therefore, changing the source position will induce a phase shift on the antinode factor and change the coupling conditions between the source and the cavity modes. To further analyze this point, we calculated in Fig. 9 (b) the photonic weights of each guided mode in the two cases (fraction of the guided energy they carry [4]). Despite the additional peaks when considering the whole active region, odd modes only carry negligible fractions of the guided energy (~1%). Besides, we can note that the photonic weights of the even modes remain quasi-constant, which suggests that in those range of thicknesses of the active region, the coupling conditions only slightly depend on the position of the source.

More generally, by differentiating the phase shift of the antinode factor φ_c over the source position (see Eq. (27)), one can easily find that $d\varphi_c = -\pi cos(\theta_e)\frac{dz_{ext}}{\lambda/4n_e}$. Thus, as a rule of thumb, we can highlight that as long as the thickness of the active region is small enough compared to $\lambda/4n_e$ (~50 nm in this case), the coupling between the source and the guided modes happens as if we only considered a single emitter centered in the active region. Let us recall that in our example the thickness of the active region is 40 nm, which is small enough for the single-dipole approximation to be accurate. We can also note that these considerations match with the standard design rules used for resonant-cavity light-emitting diodes (RCLEDs), where active regions are made less than $\lambda/4n_e$ to ensure that all emitters may be positioned at or near the antinode of the standing electric field inside the cavity [17].

For devices with larger active regions, it is also worth noticing that since the variations of the antinode factor are cosinus-dependent on the emission angle, the coupling conditions of low-order guided modes will be less impacted than the ones of high-order modes.

Let us add that the internal emission is only slightly modified in the extraction cone when considering the whole active region as shown in Fig. 9(a).

OPTICS CONTINUUM

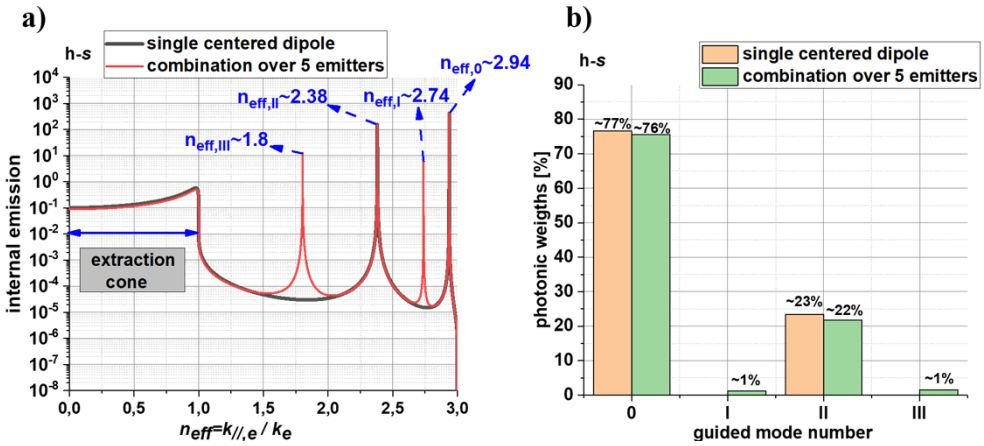

Fig. 9. s-polarized light from horizontal dipoles. Internal emission per unit solid angle as a function of the effective index and the corresponding photonic weights for a single centered dipole and combined results over 5 emitters.

It appears from this example that a good insight into the design guidelines of a multilayer structure, whether it embeds a single dipole emitter or multiple dipoles, could be gained using our model. We have also pointed out that in structures where the active region is thinner compared to a quarter-wavelength, the emitting layer can quite accurately be simulated by a single dipole centered in the active region. On the other hand, for structures with larger active regions, this particular approximation will only hold for low-order modes. For other more complex structures, any type of spatial distribution of emitters should be accounted for using the incoherent combination described in subsection 5.2.

6.1.3. Spectrally broadened single-plane emitters

In this section, we study the impact of the emission line shape on the results of section 6.1.1 where a monochromatic source was considered.

For this example, we keep the same structure as in the previous subsections. We consider a single polychromatic source plane centered in the slab. The input emission spectrum has a peak emission wavelength of 640nm and a full width at half-maximum (FWHM) of 20nm as depicted in Fig. 10(a) and similarly to the devices in [13]. Except with the angular internal emission, *s*- and *p*-polarizations are combined using the equations provided in section 5. In this case, only light going out in the ambient layer 1 is considered (see Fig. 6).

Figure 10(b) reports the spontaneous emission distribution as a function of the effective index for a monochromatic source (emitting at the peak emission wavelength) and for a polychromatic source. For the polychromatic source, the results are incoherently combined over the wavelengths using the equations provided in section 5.3. The results for the monochromatic source are the same as in section 6.1.1. Since, the emitter is centered in the slab, only even modes are excited by spontaneous emission represented by sharp peaks outside the extraction cone. However for the polychromatic source, the internal emission shape is quite altered. Indeed, for instance the sharp peaks representing the guided modes are now broadened into Lorentzian-shape functions, with a broadening that decreases as the order of the guided modes decreases. In addition, the emission shape inside the extraction cone is also impacted. These changes can be understood as follows. Both the denominator of the Airy function and antinode factor depend on the wavelength and will experience a phase shift when the wavelength is modified. The former will lead to an effective-index shift around the ones of the peak emission wavelength, while the latter will

OPTICS CONTINUUM

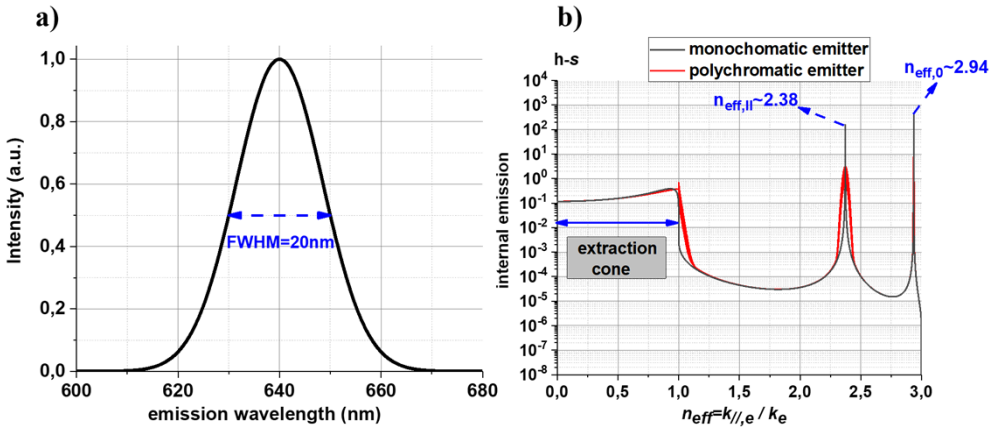

Fig. 10. s-polarized light from horizontal dipoles. a) Input emission spectrum. b) Internal emission per unit solid angle as a function of the effective index for the peak emission wavelength and for combined results over the input spectrum.

simultaneously decrease the coupling efficiency between the mode and spontaneous emission. This is the reason why each sharp peak is broadened symmetrically and has a broadening which thus depends on the FWHM of the source.

It is also worth noticing that by differentiating the phase shift of the antinode factor φ_c over the wavelength (see Eq. (27)), one easily finds that:$d\varphi_c \propto -\frac{cos(\theta_e)}{\lambda^2}d\lambda$. The phase shift of the antinode factor (and also of the Airy function) is thus cosinus-dependent on the emission angle, which explains why low-order guided modes were less impacted by the broadening than high-order ones. Similarly to what we have seen in the previous section, the shape of the internal emission inside the extraction is also slightly modified.

It thus appears that an additional asset of our model is its ability to account for the emission line shape of polychromatic light sources using incoherent combinations. This could be very useful for various incoherent light-emitting devices with emitters having non-negligible FWHM. It is also worth noticing that in some cases, a polychromatic source can be accurately simulated by a monochromatic source emitting at its peak emission wavelength. Care should however be given to the modal analysis, because high-order modes are more affected by this approximation than low-order ones.

We can finally note that spectrally-spread sources with a spatial distribution can also be accounted for in this framework by combining the two previous considerations, as described in the flow chart of Fig. 5.

6.2. *High-index slab on a substrate*

In the examples of subsection 6.1, the high-index slab was placed in vacuum. In real-life devices, light-emitting structures often lie in asymmetric optical environments with substrates (native substrates after epitaxy or receiving substrates after process) and superstrates on either side of the stack [1]. In this section, we investigate how the presence of a substrate impacts spontaneous emission distribution among cavity modes. The structural parameters are the same as before. A single monochromatic dipole is centered inside the cavity. However, our test structure is now made of a substrate of index $n_2 = 1.45$ considered transparent and an air superstrate ($n_1 = 1$).

Figure 11 displays the total internal emission (on both sides of the structure) as a function of the effective index for both *s*- and *p*-polarizations.

OPTICS CONTINUUM

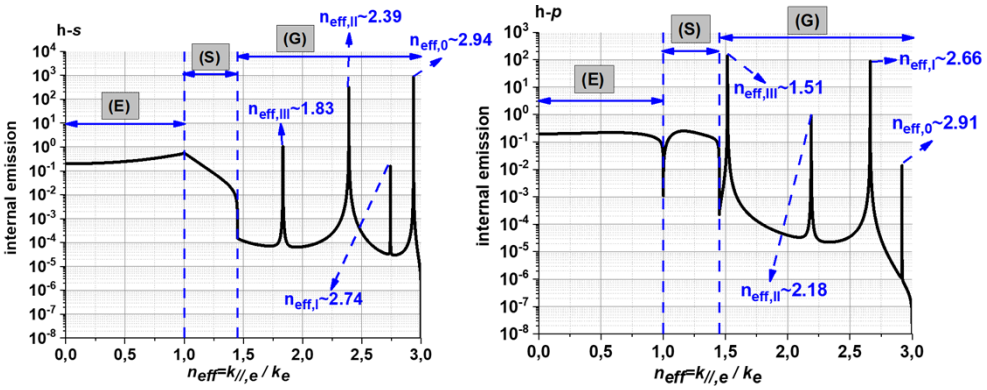

Fig. 11. s- and p- polarized light from horizontal dipoles. Internal emission per unit solid angle as a function of the effective index. E = directly emitted light, S = substrate light, G = guided light.

As can be seen, the angular distribution of spontaneous emission becomes a bit more intricate. Indeed, light emitted by the dipole can couple to different types of modes. A fraction of the emitted light, which is in the air cone ($n_{eff} < 1$), directly radiates in the air. This is the so-called directly emitted light and amounts to ~17% of the total emitted light in this case (s- and p-polarized light combined). Another fraction of the emitted light (~12%) is propagative in the transparent substrate but not in air ($1 < n_{eff} < 1.45$). This is the so-called substrate light and accounts for most of the emitted light in a basic mounted LED for lighting applications, where reflectors are placed on the top side of the structure to favor bottom emission (towards the transparent substrate) [21]. Finally, most of the emitted light excite the guided modes available in the cavity, which are represented by sharp peaks outside the air and substrate cone ($n_{eff} \geq 1.45$). This is the so-called guided light and amounts to ~71% of the total emitted light due to the high refractive index of the slab. In most of LEDs, this light is one of the main efficiency bottlenecks, since it does not go out and will eventually be lost for instance by non-radiative re-absorption.

It is worth noticing that to devise an adequate strategy for circumventing these efficiency issues, one needs an accurate evaluation of the amounts of light that couple to the different cavity modes. This highlights the key importance of the herein-developed model.

A large number of strategies have already been implemented in the literature for that matter. Some of them rely on light extractors such as photonic-crystals to diffract this guided light out of the structure [1]. In other cases, the devices are transferred from their native substrates onto receiving substrates with back reflectors to favor top emission by redistributing spontaneous emission [17]. This latter strategy will be further investigated in the next example using our model.

6.3. High-index slab with a distributed Bragg reflector

In this last example, we investigate the possibility of using bottom reflectors for adequately redistributing spontaneous emission while harnessing the substrate light. This helps favor top emission and shows the applicability of our model to more complex multilayer structures. The same high-index slab is thus placed on top of a distributed Bragg reflector (DBR) consisting of 3 pairs of alternate indices of 1.4 and 2. The main design parameter which governs both radiation distribution and LEE in these structures is the cavity detuning. It evaluates the discrepancy between the cavity thickness and its optimal value for a Fabry-Pérot (FP) resonance at normal incidence [22]. The initial cavity thickness is chosen so that the cavity order is $n_e d_e/\lambda=1$ to better visualize cavity effects. Subsequently, we interleaved a tuning layer (denoted *gap*) whose

OPTICS CONTINUUM

thickness is varied to adjust the overall thickness of the cavity and investigate how tuning and detuning the cavity impacts the performances of these kinds of devices. The corresponding schematics is displayed in Fig. 12.

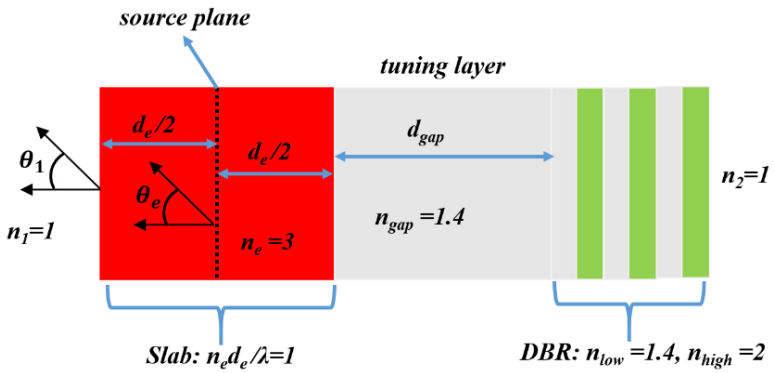

Fig. 12. Schematics of the high-index slab with a bottom Distributed Bragg reflector consisting of 3 pairs of alternate indices 1.45 and 2. The emitter is a horizontal dipole centered inside the cavity.

6.3.1. Impact of the detuning on LEE and directionality

The light source is a single monochromatic horizontal dipole centered inside the slab. Only light going out in the ambient medium 1 (denoted "*top side*") is considered. Figure 13 displays LEE and farfield emission pattern as a function of the thickness of the tuning layer (in number of $\lambda/4n_{gap}$). In both cases, *s*- and *p*-polarizations are combined using the equations provided in section 5.

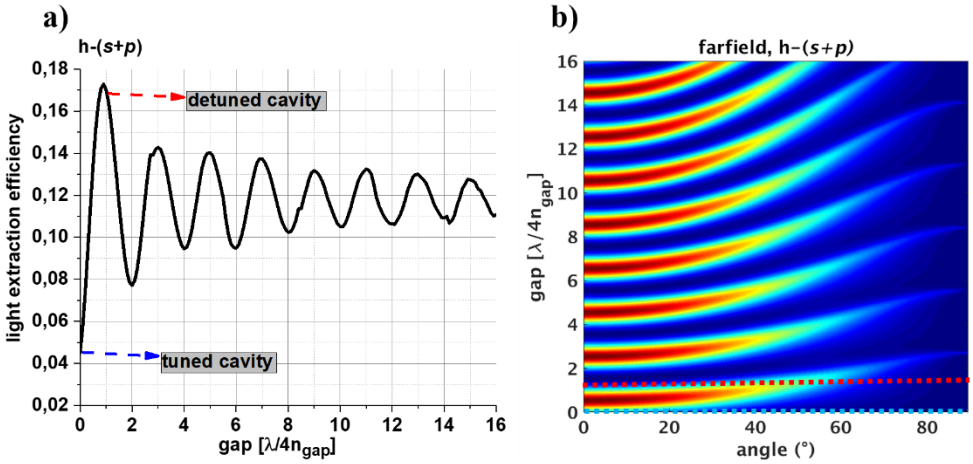

Fig. 13. Horizontal dipole (s- and p-polarizations combined). a) LEE and b) farfield patterns as a function of the thickness of the tuning layer. Blue and red dashed lines indicate gaps corresponding to a tuned and detuned cavity, respectively.

We can see that light extraction efficiency is at its lowest value without the tuning layer (~4% at $d_{gap}=0$). Next, as its thickness is adjusted, LEE reaches its highest value (~16%) at around $\lambda/4n_{gap}$ and then oscillates with a $\lambda/2n_{gap}$ periodicity and an oscillation amplitude that tends to

OPTICS CONTINUUM

decrease as thickness of the tuning layer increases. Those oscillations eventually start to smear out for large values of gaps, when the DBR only weakly interacts with the cavity modes. It is worth noticing that the maxima and minima of LEE are not arbitrarily located, but rather they regularly occur at around $(2p + 1)\ \lambda/4n_{gap}$ and $(2p)\ \lambda/4n_{gap}$, respectively (with p an integer).

Looking now at the farfield emission pattern in Fig. 13(b), we can observe the common "boomerang"-shaped lines, which are typical evidences of Fabry-Pérot (FP) interferences inside the cavity [17]. Without the tuning layer, the farfield is highly directional with a peak angle around the normal incidence. As the thickness of the tuning layer increases, the farfield shape oscillates between directional and non-directional patterns, with a peak emission angle that can reach ~42°. We can note that the minima of LEE occur at gaps corresponding to highly directional farfields. However, when the thickness of tuning layer is adjusted to obtain high LEE at around $(2p + 1)\ \lambda/4n_{gap}$, the peak angle is shifted from normal incidence to ~42°, which results into a non-directional farfield.

We further analyze this latter point by plotting spontaneous emission distribution inside the cavity (towards the top side of the structure) for the two values of gaps highlighted in Fig. 13 (gaps of 0 and ~1). As shown in Fig. 14(a), when the gap equals zero (and more generally $(2p)\ \lambda/4n_{gap}$), the cavity parameters are tuned so that the main FP mode occurs at normal incidence. As a result, we obtain in the outside medium a highly directional farfield pattern as displayed in Fig. 14(b), where the radiation patterns are normalized by their maximum values for the sake of clarity. The corresponding LEE is however at its lowest value (~4%) because the overall integral of the internal emission inside the air cone is not optimized. When its thickness is adequately adjusted to reach maximum LEE (~16%), the cavity becomes detuned which shifts the main FP lobe from normal incidence to ~13°. The resulting farfield radiation pattern, sometimes described as 'rabbit's ears' because of its appearance, becomes less directional than the previous one (see Fig. 14(b)). Thus, RCLED-like structures have to be optimized for specific applications, either by maximizing extraction efficiency with a non-directional emission pattern or by optimizing brightness (e.g. for coupling to optical systems with limited numerical apertures).

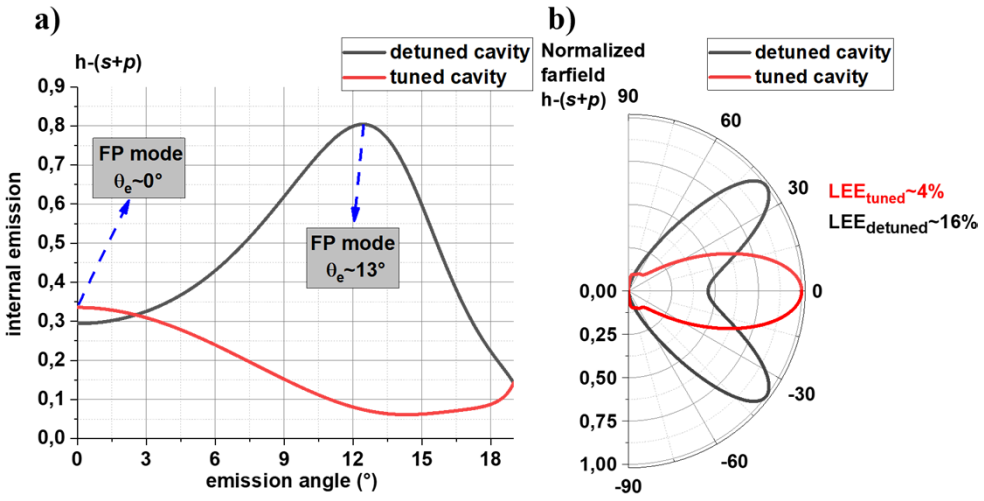

Fig. 14. Horizontal dipole (s- and p-polarizations combined). a) Angular internal emission distribution within the extraction cone and b) normalized farfield patterns for tuned and detuned cavity.

OPTICS CONTINUUM

6.3.2. Spectral redistribution due to cavity effects

In the previous example, radiation dynamics was only analyzed for one wavelength. Although, the combined farfield radiation patterns provided a good insight into the emission distribution, they failed to depict the behavior per wavelength of the emission spectrum. In this example, we analyze how the intrinsic emission spectrum is modified due to cavity effects. The multilayer structure is the same as before with a single polychromatic horizontal dipole lying in the middle of the slab. Its intrinsic emission spectrum is Gaussian-shaped with a peak emission wavelength at 640nm and a FWHM of 20nm. We investigate a tuned cavity ($gap = 0$) and a detuned cavity ($gap = \lambda/4n_{gap}$) as explained before, in this case λ being the peak emission wavelength. In those two configurations, *s*- and *p*-polarizations are combined and only light going out into the top side of the structure is considered. Figure 15 depicts the normalized spectrally-resolved farfield (SRF) patterns for the tuned and detuned cavities, calculated using Eq. (36) of section 5.3.

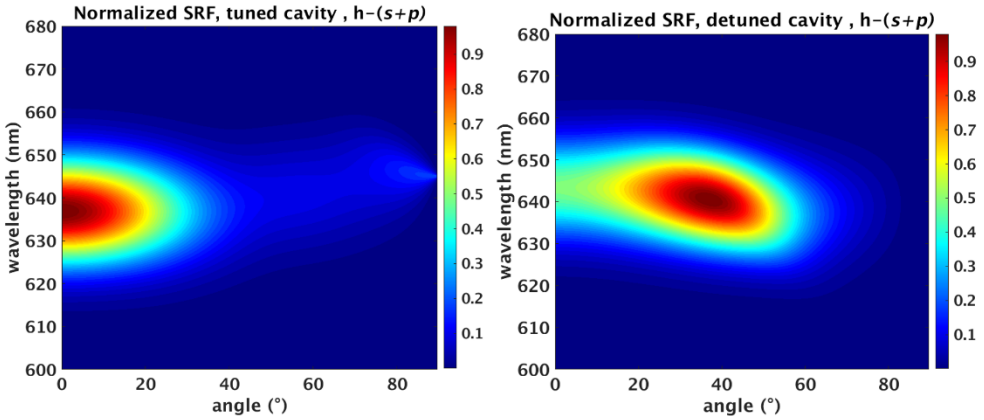

Fig. 15. Horizontal dipole (s- and p-polarizations combined). Normalized spectrally-resolved farfield patterns for a tuned and detuned cavity.

From those *SRF* patterns, we calculated the output spectra using Eq. (37) within the full collection angle (where all the emitted light collected) and within an acceptance angle of 20°. Those results are shown in Fig. 16. Each of the emission wavelength experiences its own interference conditions since both antinode factor and Airy function are wavelength-dependent as seen previously. For the tuned cavity, the maximum extraction efficiency is not reached at the peak emission wavelength due to the tuning conditions. This yields a spectral redistribution of spontaneous emission when going out of the cavity. Subsequently, this induced a blue shift of ~0.8 nm between the input and the output spectrum (with the full collection angle) as depicted in Fig. 16(a), which is accompanied with an increase of the FWHM of ~2.4 nm. In addition, despite the fact that the most intense FP lobe is around the normal incidence, we can observe the presence of an additional peak in the SRF located at around 80°. This peak stems from the additional FP mode that is present at the edge of the extraction cone in Fig. 14(a). Although its intensity is lower, its corresponding solid angle is higher than the one of the main lobe located at normal incidence. Therefore, both the shape and the distribution of the output spectrum are angle-dependent. For instance, we can observe a blue shift of ~2.4 nm and a FWHM which decreases by ~2.4 nm between the output spectra collected within angles of 90° and 20°.

For the detuned cavity on the other hand, since the maximum LEE is reached at the peak emission wavelength, the shift between the input and output spectra is alleviated as displayed in Fig. 16(b). However, since the main FP mode is extracted at an angle around 42° (see Fig. 15), the output spectra becomes clearly angle-dependent. The FWHM between the output spectra

OPTICS CONTINUUM

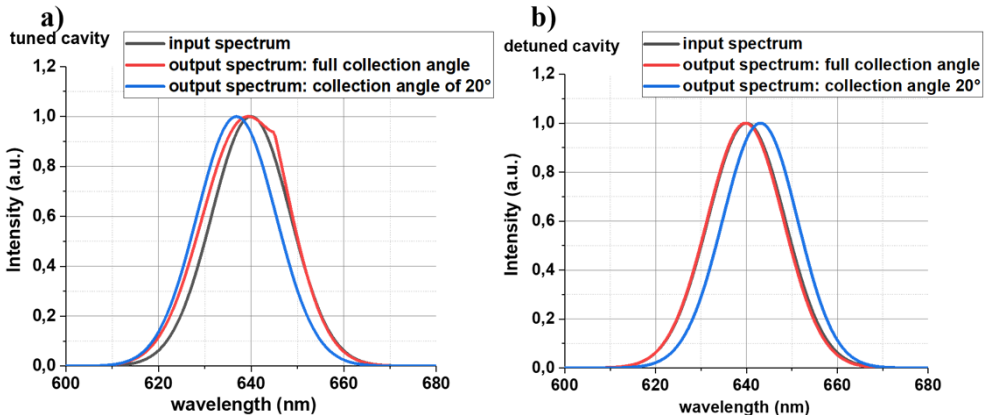

Fig. 16. Input and output emission spectra for a) tuned and b) detuned cavities. The output spectra within a collection angle of 20° are also added

collected within angles of 90° and 20° remain unchanged; nevertheless, there is a red shift of ~3.6nm between those two.

The aforementioned cavity effects are all the more visible that the FHWM of the intrinsic emission spectrum is high and more intricate output emission spectra with many peaks have already been reported for RCLEDs [22].

We have thus shown in this particular example that the herein-developed model can help gain a good insight into the radiation dynamics of dipoles embedded in complex multilayer structures and provide meaningful design guidelines, which are of key interest in optoelectronics.

7. Conclusion

We have proposed a novel full-matrix algebraic framework for modeling dipole emission modification in layered media. This formalism has the specificity of generalizing the standard 2×2 transfer-matrices into a compact 3×3 framework, which thus allowed us to treat dipole radiation directly into the matrix formulation as a source matrix.

This model has been thoroughly developed for the case of spontaneous emission in stratified media and all the corresponding equations necessary to evaluate the key figure of merits for designing incoherent light-emitting structures have been provided. It has also been extended to configurations with complex emitter regions with both spectral and spatial distributions using herein-proposed formulas for incoherent combination.

We have found a very good agreement between our model and rigorous electromagnetic simulations using incoherent 3D-FDTD, which confirms its accuracy. It has then been applied to various examples to demonstrate its applicability: firstly to polychromatic distributed emitters in a high-index slab placed in vacuum and then to a high-index slab with DBR mirors to investigate the impact of the cavity tuning and detuning on device performances.

Since it only requires modest computational efforts, we hope that this model can help better understand spontaneous emission dynamics in layered media and thus pave the way to novel design guidelines for devices in many fields of optoelectronics.

Funding. Horizon 2020 Framework Programme (755497).

Disclosures. The authors declare no conflicts of interest.

Data availability. Data underlying the results presented in this paper are not publicly available at this time but may be obtained from the authors upon reasonable request.

OPTICS CONTINUUM

References

1. A. Ndiaye, A. Ndiaye, A. Ghazouani, C. Seassal, E. Drouard, N. Olivier, and B. B. Bakir, "Enhanced light-extraction efficiency and emission directivity in compact photonic-crystal based AlGaInP thin-films for color conversion applications," Opt. Express **29**(22), 35965–35979 (2021).
2. E. F. Schubert, *Light-Emitting Diodes*, 2nd ed. (Cambridge University Press, 2006).
3. H. Benisty, R. Stanley, and M. Mayer, "Method of source terms for dipole emission modification in modes of arbitrary planar structures," J. Opt. Soc. Am. A **15**(5), 1192–1201 (1998).
4. A. Ndiaye, H. S. Nguyen, C. Seassal, E. Drouard, and B. Ben Bakir, "Farfield pattern and guided-mode extraction analysis for highly directional emission from photonic-crystal based AlGaInP/InGaP MQW color-converters in thin-film geometry," AIP Adv. **12**(4), 045122 (2022).
5. C.-F. Lai, C.-H. Chao, and W.-Y. Yeh, "Optimized Microcavity and Photonic Crystal Parameters of GaN-Based Ultrathin-Film Light-Emitting Diodes for Highly Directional Beam Profiles," IEEE Photonics Technol. Lett. **22**(21), 1547–1549 (2010).
6. W. Lukosz, "Theory of optical-environment-dependent spontaneous-emission rates for emitters in thin layers," Phys. Rev. B **22**(6), 3030–3038 (1980).
7. M. Born and E. Wolf, *Principles of Optics: Electromagnetic Theory of Propagation, Interference and Diffraction of Light*, 7th ed. (Cambridge University Press, 1999).
8. K. Kang, Y. Lee, and B. Yang, "A Generalized Fabry–Pérot Formulation for Optical Modeling of Organic Light-Emitting Diodes Considering the Dipole Orientation and Light Polarization," IEEE Photonics Journal, **8**(2), 1– 19 (2016).
9. W. Lukosz and R. E. Kunz, "Light emission by magnetic and electric dipoles close to a plane dielectric interface. II. Radiation patterns of perpendicular oriented dipoles," J. Opt. Soc. Am. **67**(12), 1615–1619 (1977).
10. W. Lukosz, "Light emission by magnetic and electric dipoles close to a plane dielectric interface. III. Radiation patterns of dipoles with arbitrary orientation," J. Opt. Soc. Am. **69**(11), 1495–1503 (1979).
11. J. Kim, K.-Y. Kim, and J. Kim, "Generalized Poynting vector model to calculate the spatial and spectral profiles of the electric field intensity, optical power flow, and optical absorption for all optical modes of organic light-emitting diodes," Opt. Express **27**(16), A1261–A1286 (2019).
12. P. Royo, R. P. Stanley, and A. Ilegems, "Analytical calculation of the extraction efficiency of microcavity light-emitting diodes for display and fiber coupling applications," IEEE J. Sel. Top. Quantum Electron. **8**(2), 207–218 (2002).
13. A. Ndiaye, H. S. Nguyen, A. Ghazouani, C. Seassal, E. Drouard, N. Olivier, and B. B. Bakir, "Enhanced conversion efficiency and tailored radiation patterns assisted by photonic-crystal light-extractors in compact MQW based color-converters for µLED applications," in *Light-Emitting Devices, Materials, and Applications XXVI* (SPIE, 2022), 12022, pp. 167–175.
14. M. Chakaroun, A. T. Diallo, S. Hamdad, S. Khadir, A. P. A. Fischer, and A. Boudrioua, "Experimental and Theoretical Study of the Optical Properties Optimization of an OLED in a Microcavity," IEEE Trans. Electron Devices **65**(11), 1–8 (2018).
15. C.-F. Lai, J.-Y. Chi, H.-C. Kuo, H.-H. Yen, C.-E. Lee, C.-H. Chao, H.-T. Hsueh, and W.-Y. Yeh, "Far-field of GaN film-transferred green light-emitting diodes with two-dimensional photonic crystals," Opt. Express **17**(11), 8795–8804 (2009).
16. H. S. El-Ghoroury, M. Yeh, J. C. Chen, X. Li, and C.-L. Chuang, "Growth of monolithic full-color GaN-based LED with intermediate carrier blocking layers," AIP Adv. **6**(7), 075316 (2016).
17. P. M. Pattison, A. David, R. Sharma, C. Weisbuch, S. DenBaars, and S. Nakamura, "Gallium nitride based microcavity light emitting diodes with 2λ effective cavity thickness," Appl. Phys. Lett. **90**(3), 031111 (2007).
18. H. Benisty, H. De Neve, and C. Weisbuch,"Impact of planar microcavity effects on light extraction-Part II: selected exact simulations and role of photon recycling,"IEEE Journal of Quantum Electronics **34**(9), 1632–1643 (1998).
19. "Impact of photonic crystals on LED light extraction efficiency: approaches and limits to vertical structure designs - IOPscience," https://iopscience.iop.org/article/10.1088/0022-3727/43/35/354005.
20. S. Che, A. Yuki, H. Watanabe, Y. Ishitani, and A. Yoshikawa, "Fabrication of Asymmetric GaN/InN/InGaN/GaN Quantum-Well Light Emitting Diodes for Reducing the Quantum-Confined Stark Effect in the Blue-Green Region," Appl. Phys. Express **2**(2), 021001 (2009).
21. D.-S. Han, J.-Y. Kim, S.-I. Na, S.-H. Kim, K.-D. Lee, B. Kim, and S.-J. Park, "Improvement of light extraction efficiency of flip-chip light-emitting diode by texturing the bottom side surface of sapphire substrate," IEEE Photonics Technol. Lett. **18**(13), 1406–1408 (2006).
22. J. Dorsaz, J.-F. Carlin, C. M. Zellweger, S. Gradecak, and M. Ilegems, "InGaN/GaN resonant-cavity LED including an AlInN/GaN Bragg mirror," phys. stat. sol. (a) **201**(12), 2675–2678 (2004).